Available online at www.sciencedirect.com
SCIENCE DIRECT®
Journal of Nuclear Materials 336 (2005) 323–330
journal of nuclear materials
www.elsevier.com/locate/jnucmat

Characterization of defect clusters in ion-irradiated A533B steel

K. Fujii *, K. Fukuya

Institute of Nuclear Safety System Inc., 64 Sata, Mihama-cho, Mikata-gun, Fukui 919-1205, Japan

Received 26 December 2003; accepted 4 October 2004

Abstract

A weak-beam transmission electron microscopy study was carried out for matrix damage in A533B reactor pressure vessel (RPV) steel produced by 3 MeV Ni^{2+} ion irradiation to a dose of 1 dpa at 290 °C. The matrix damage was found to consist of small dislocation loops. The observed and analyzed dislocation loops have Burgers vectors $\boldsymbol{b} = a\langle 1\,0\,0\rangle$. The dislocation loops have a mean image size $d = 2.5$ nm and the number density is about $1 \times 10^{22}\,m^{-3}$. Most of the loops are stable after thermal annealing at 400 °C for 30 min. This indirect evidence suggests that their nature is interstitial.

PACS: 61.80; 61.72.F; 61.40.X; 81.40.N; 06.60.E

1. Introduction

Radiation embrittlement of RPV steels is one of the critical issues for integrity and safety in long-life operation of light water reactors. The embrittlement is attributed to nano-scale microstructural features such as copper rich precipitates, matrix damage and grain boundary segregation [1,2]. Mechanical property studies on RPV steels containing different levels of copper have indicated that matrix damage is the dominant feature for hardening in low Cu steels and at high fluences in high Cu steels [3,4]. However, the exact nature of this component of the damage in irradiated commercial steels has not been clarified yet by direct characterization using transmission electron microscopy (TEM). The available evidence from direct and indirect techniques, as well as from theoretical studies indicates that the matrix damage consists of irradiation-induced point-defect clusters, such as interstitial loops, micro-voids and/or vacancy loops. Small dislocation loops have been observed using TEM in neutron and ion-irradiated iron [5–10].

The direct observation of small defect clusters in ferrous materials using TEM is difficult due to the high magnetism, the complication of the microstructure and the technical difficulty of preparing a TEM foil because of the high sensitivity to oxidation. However, weak-beam microscopy is fruitful for observation of point-defect clusters, and has been shown capable of reliably identifying and sizing dislocation loops as small as 1–2 nm [11,12].

In this study, heavy ion irradiation experiments were carried out to induce sufficient matrix damage for the point-defect clusters to grow to a size that is visible using TEM. Thin foil specimens were prepared using focused ion beam (FIB) methods. We present the results of a weak-beam microscopy study of matrix damage in the

* Corresponding author. Tel.: +81 770 37 9114; fax: +81 770 37 2009.
E-mail address: fujiik@inss.co.jp (K. Fujii).

0022-3115/$ - see front matter
doi:10.1016/j.jnucmat.2004.10.090

A533B steel samples following irradiation by 3 MeV Ni^{2+} ions to a dose of 1 dpa at 290 °C.

2. Experimental

Sample blocks of A533B steel were used in this study. The chemical composition is shown in Table 1. Coupons measuring $35 \times 9 \times 0.2$ mm were cut out from the blocks, and the surfaces were mechanically polished using wet grinding on SiC papers down to 1200 grit. After diamond polishing with 3, 1 and 1/4 μm particle size, the remaining cold-worked surface regions were removed with chemical polishing using 5% hydrofluoric acid, 85% hydrogen peroxide and 10% distilled water, at 0 °C.

Ion irradiation was performed using a tandem implanter at Materials Diagnostics, USA. A 3 MeV Ni^{2+} ion beam was used to irradiate samples. The irradiation temperature was 290 ± 3 °C, and was measured using a thermocouple spot-welded to the sample. The ion flux and fluence were 1.6×10^{11} ions/cm^2/s and 1.6×10^{15} ions/cm^2, respectively. The corresponding calculated dose rate and dose-calculation using the SRIM2000 program in pure Fe with the displacement energy $E_d = 40$ eV [13] were 1.0×10^{-4} dpa/s and 1.0 dpa at a depth of 300 nm, respectively. The implanted Ni ion concentration was estimated as 0.002 wt% at the depth of 300 nm. This amount is much smaller than the original Ni content of 0.57 wt% and thus, the effect of the implanted Ni ions on the microstructure change is negligible. The Ni ions are implanted as interstitials. The flux of the implanted Ni ions at a depth of 300 nm was estimated as 2×10^{-9} ions/atoms/s. This rate is much smaller than that of point defects produced by the displacement (1×10^{-4} dpa/s). The effect of the implanted Ni ions on nucleation and growth of point-defect clusters will be negligible. As an additional experiment, post-irradiation annealing was carried out at 400 °C for 30 min in vacuum in order to indirectly determine the vacancy or interstitial nature of irradiation-induced point-defect clusters.

Thin foils suitable for TEM observation were prepared using a focused ion beam (FIB) system (HITACHI FIB-2000A). Details of the foil machining processes are as follows. Small specimens measuring $2 \times 1 \times 0.2$ mm were cut out from the irradiated sample. The backside of the irradiated surface was mechanically polished to a thickness of about 0.02 mm in order to decrease the magnetic field of the specimen. The thin specimens were fixed on the V-shaped grids using glue, and mounted in the FIB system. FIB processing using a Ga ion beam with an accelerating voltage of 30 kV was used to process a damage region into an electron transparent foil in two ways: cross-sectional processing, and selected depth processing. The cross-sectional processing was used to process the whole damage region to a depth of about 1 μm depth into a thin foil and the distribution of irradiation-induced point-defect clusters could be observed. In this study, the cross-sectional foils were inclined at 20° with respect to the irradiated surface. At this angle the defect distribution is effectively magnified by about three times compared to the actual depth profile. The selected depth processing was used to examine damage at a selected depth in a thin foil. Thus analysis of the matrix damage was carried out at a depth of 300 nm. Normal FIB processing prepares a wedge-shaped foil, but in this experiment, final FIB processing was carried out under the condition that the foil was tilted at about ±1° in order to reduce the wedge-shape of the thin foil.

FIB processing produces damage in the surface region of a specimen. SRIM2000 calculation for 30 keV Ga irradiation of pure Fe showed that peak and maximum iron ranges were about 4 and 20 nm, respectively. It is necessary to remove this FIB damage in order to observe the underlying irradiation-induced point-defect clusters. In this study, flash electrolytic etching was carried out to remove the FIB damage. Details of the flash etching are as follows. A beaker method was used. The etchant was 2% perchloric acid and 98% methanol, and the etchant temperature was less than −60 °C. The applied voltage was 20 V. The distance between the specimen and the stainless steel cathode was about 50 mm. Fig. 1 shows the effect of the flash etching for the removal of the FIB damage layers. Fig. 1(a) and (b) shows the bright-field and weak-beam dark-field TEM images, respectively, taken from the same area of the thin foil prepared by only FIB processing in an unirradiated reference specimen. The damage microstructure produced by the FIB processing was observed as black and/or white dots in these figures. Fig. 1(c) and (d) shows the TEM images taken from the same area of another thin foil prepared by FIB processing and the flash etching for 0.01 s. Only line dislocations were identified and no damage by FIB processing was observed. This result demonstrates that the FIB damage layers were successfully removed by the flash etching for 0.01 s. From the result of experi-

Table 1
Chemical composition (wt%)

C	Si	Mn	P	S	Ni	Cr	Mo	Cu	Fe
0.18	0.23	1.39	0.007	0.008	0.57	0.03	0.46	0.03	Balance

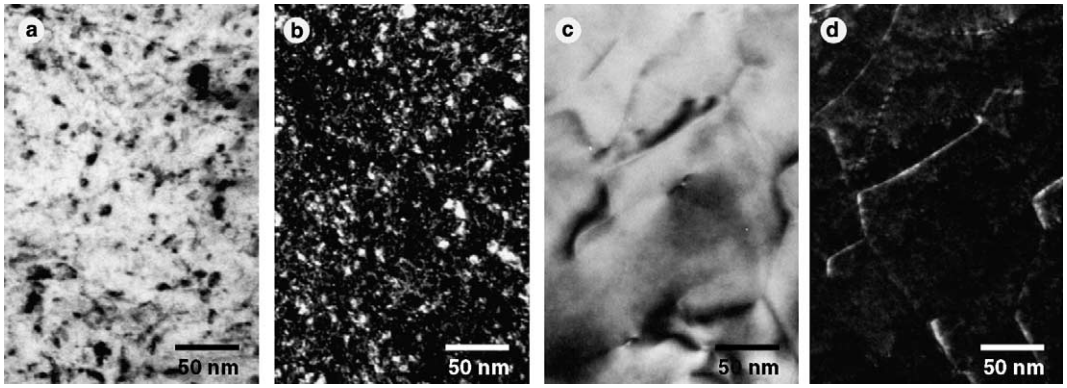

Fig. 1. Effect of flash etching for removal of FIB damage layers. (a,b) The bright-field and weak-beam dark-field TEM images taken from a same area of the thin foil prepared by only FIB processing in unirradiated reference specimen. (c,d) The TEM images taken from a same area of another thin foil prepared by FIB processing and the flash etching for 0.01 s.

ments for measuring the decrease of thickness of thin foils with flash etching using a simple convergent-beam technique [14], the decreases of thickness with the flash etching for 0.01 s was 100–120 nm. This amount was enough to remove the FIB damage region without affecting the underlying matrix damage.

The specimens were examined in a HITACHI HF-3000 field emission gun transmission electron microscope at 300 kV, immediately after the flash etching in order to minimize oxidation. Grains with orientations close to [0 1 1] and [0 0 1] were chosen for analysis. Weak-beam microscopy was employed to characterize the matrix damage. The contrast under weak-beam conditions of an individual defect may depend on the exact imaging conditions. However, by recording images at several different values of the deviation parameter s_g, it is possible to reliably identify and size dislocation loops as small as 1–2 nm [11]. Sizes of over 100 individual defects were measured. Defect number densities were measured using values of the local foil thickness estimated from a simple convergent-beam technique [14]. Weak-beam contrast experiments using reflections with diffraction vector $\boldsymbol{g} = 0\,1\,\bar{1}$, $\boldsymbol{g} = 2\,1\,\bar{1}$, $\boldsymbol{g} = 2\,0\,0$ and $\boldsymbol{g} = 2\,\bar{1}\,1$ close to [0 1 1] pole and $\boldsymbol{g} = \bar{1}\,1\,0$, $\boldsymbol{g} = 0\,2\,0$, $\boldsymbol{g} = 1\,1\,0$ and $\boldsymbol{g} = 2\,0\,0$ close to [0 0 1] pole were used to gain information on the loop Burgers vectors $\boldsymbol{b}$. Over 100 defects were analyzed by following their contrast in different reflections.

3. Results and discussion

TEM images of a cross-sectional foil are shown in Fig. 2. The thin layer at the top surface was lost to the foil by the flash etching process. However, W-deposition on the incident surface, before FIB processing in order to protect the surface from the beam and to provide a surface marker, remained and enabled the top surface to be identified. The transformed scale for the depth from the irradiated surface is shown in the low magnification micrograph of Fig. 2(a). Dislocations and precipitates such as carbides can be clearly observed in the whole image. Small (<10 nm) black dots were observed only in the region up to about 1 μm depth. Fig. 2(b)–(d) shows the enlarged details of the areas within the rectangle marked in Fig. 2(a). Small black dots were observed in Fig. 2(b) enlarged from the area of about 0.3–0.5 μm depth. Fig. 2(c) shows the area of about 0.8–1.0 μm depth. The boundary of visible black dots was observed. No black dots were observed in Fig. 2(d) enlarged from the area of about 1.2–1.5 μm depth. From the SRIM2000 calculation, the peak damage depth and damage range are about 0.8 and 1.0 μm, respectively. The depth to which small black dots were observed was consistent with the result of damage calculation.

A weak-beam image taken in $\boldsymbol{g} = \bar{1}\,1\,0$ close to the [0 0 1] pole in the foil at a depth of 300 nm is shown in Fig. 3. The matrix damage consists of small (2–6 nm) dislocation loops, which are visible in the weak-beam images as white dots. The dislocation loops are almost homogeneously distributed. Larger dislocation loops were typically observed near grain boundaries although the inhomogeneous distribution of dislocation loops, such as preferential formation on one side of dislocation lines reported by Hoelzer et al. [9], was not observed.

Fig. 4 shows weak-beam images of the same area of the foil at 300 nm depth imaged (a) with $\boldsymbol{g} = 2\,0\,0$, (b) $\boldsymbol{g} = 2\,1\,\bar{1}$, and (c) $\boldsymbol{g} = 0\,1\,\bar{1}$ close to the [0 1 1] pole. Dislocation loops in bcc metals show contrast change depending on the Burgers vector used to image them [15]. Fig. 5 shows an example of contrast analyses on dislocation loops with changing diffraction vector: (a) $\boldsymbol{g} = 0\,1\,\bar{1}$

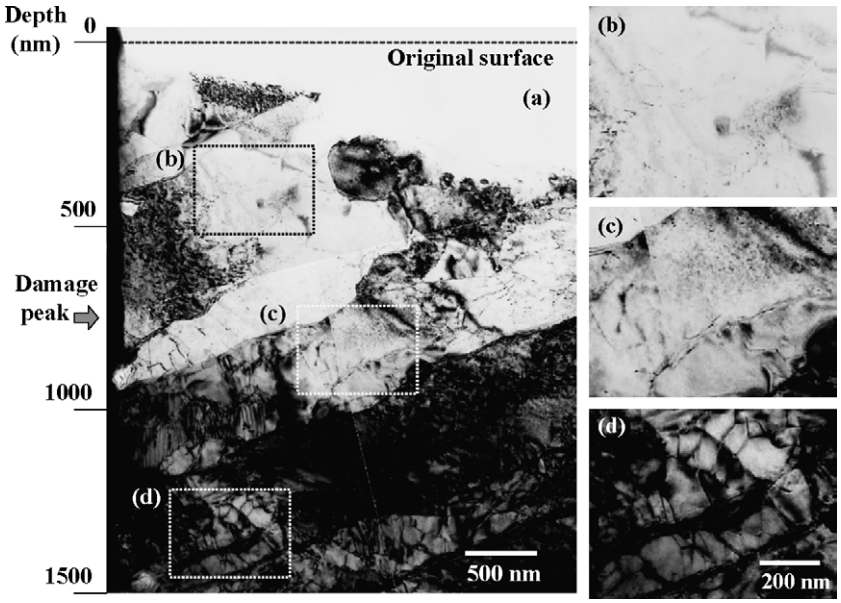

Fig. 2. TEM images of cross-sectional foil of (a) ion-irradiated whole region, and (b,c,d) enlarged detail of the areas within the rectangle marked in (a).

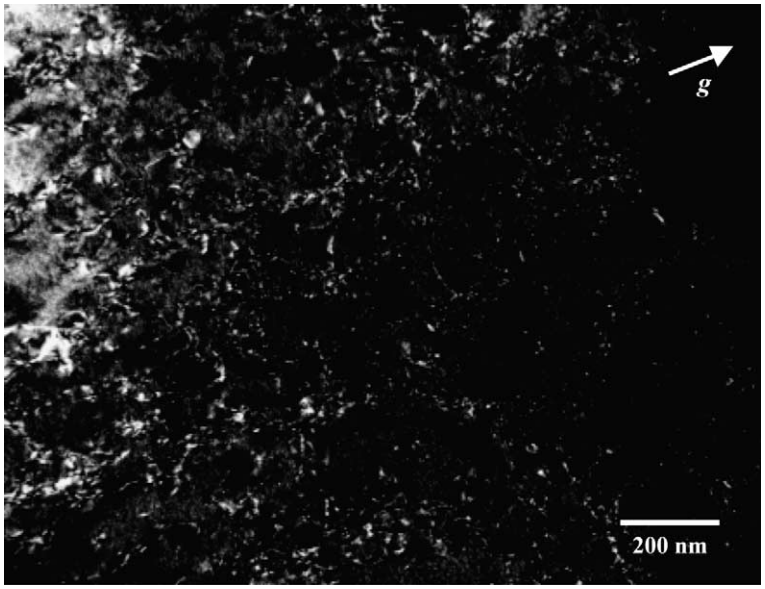

Fig. 3. A weak-beam image taken in $\boldsymbol{g} = \bar{1}\,1\,0$ close to the [0 0 1] pole in the foil at a depth of 300 nm.

and (b) $\boldsymbol{g} = 2\,0\,0$ close to the [0 1 1] pole. Two of the three loop variants with $\boldsymbol{b} = a\langle 1\,0\,0\rangle$ have $|\boldsymbol{g}\cdot\boldsymbol{b}| = 1$ and should be visible in Fig. 5(a), but these two loop variants have $|\boldsymbol{g}\cdot\boldsymbol{b}| = 0$ and should be out-of-contrast in (b). Two of the four loop possible variants with $\boldsymbol{b} = a/2\langle 1\,1\,1\rangle$ should be visible in Fig. 5(a), and all four loop variants should be visible in (b). In Fig. 5(a), the encircled white dots show the dislocation loops with typical $|\boldsymbol{g}\cdot\boldsymbol{b}| = 1$ type contrast, but these dislocation loops are out-of-contrast in Fig. 5(b). This result means that these dislocation loops have $\boldsymbol{b} = a\langle 1\,0\,0\rangle$. In this observation, about 50% of the clear and bigger white dots were subjected to contrast analyses. Based on the results of the detailed contrast analyses, most of the clearly recognized disloca-

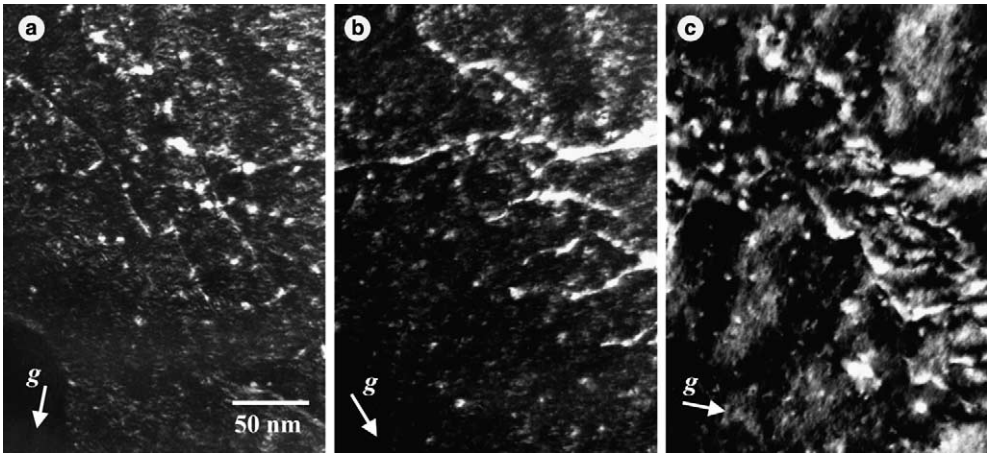

Fig. 4. Weak-beam images of the same area imaged (a) with diffraction vector $\boldsymbol{g} = 200$, (b) $\boldsymbol{g} = 21\bar{1}$ and (c) $\boldsymbol{g} = 01\bar{1}$ close to the [011] pole, in the foil at 300 nm depth.

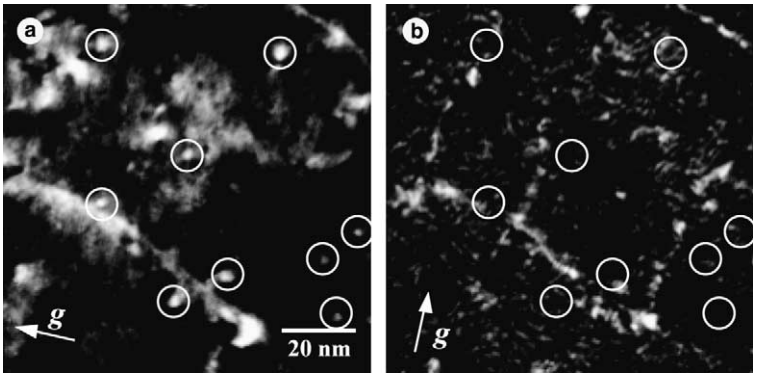

Fig. 5. Contrast analysis on dislocation loops: weak-beam images of the same area imaged (a) with diffraction vector $\boldsymbol{g} = 01\bar{1}$ and (b) $\boldsymbol{g} = 200$ close to the [011] pole, in the foil at 300 nm depth.

tion loops had $\boldsymbol{b} = a\langle 100\rangle$. The size distribution of the analyzed dislocation loops is shown in Fig. 6. The dislocation loops had a mean image size $d = 2.5$ nm. Estimates of the dislocation loop number density gave a value of about $1 \times 10^{22}\,\mathrm{m}^{-3}$. The present results have demonstrated that $a\langle 100\rangle$ dislocation loops can form in ion-irradiated A533B steels. The integrated number of point defects retained in the visible loops was calculated as $7 \times 10^{23}\,\mathrm{m}^{-3}$ from the mean diameter and number density of the visible dislocation loops to obtain a lower limit number for the fraction of Frenkel pairs retained as damage and also a lower limit number for the retained vacancy concentration. The total number of point defects produced by the irradiation of 1 dpa was calculated as $8 \times 10^{28}\,\mathrm{m}^{-3}$. The concentration of point defects retained in the visible dislocation loops represents only a small fraction of the total number produced ($\sim 2 \times 10^{-5}$). It is suggested that recombination between

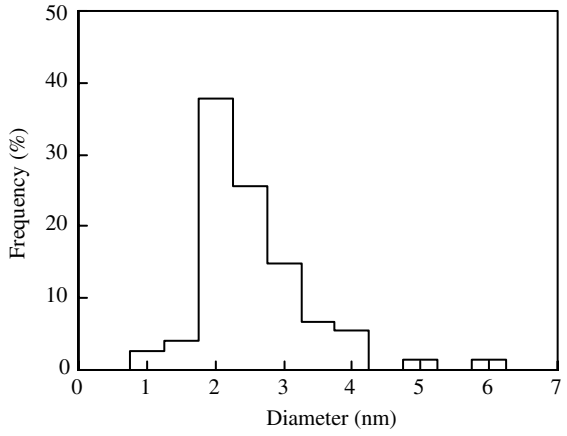

Fig. 6. Size distribution of dislocation loops under irradiation to 1 dpa at 290 °C.

vacancies and interstitials is the dominant recovery process in ion-irradiated A533B steels with the dose rate of 10^{-4} dpa/s.

In this observation of the ion-irradiated A533B steel, most of the visible dislocation loops had $\boldsymbol{b} = a\langle 1\,0\,0\rangle$. This is consistent with previous observations that a majority of dislocation loops have $\boldsymbol{b} = a\langle 1\,0\,0\rangle$ in irradiated iron [5,7–12,16], although the formation of $a/2\langle 1\,1\,1\rangle$ dislocation loops is expected to be favorable in terms of energy [17]. A nucleation model for $a\langle 1\,0\,0\rangle$ and $a/2\langle 1\,1\,1\rangle$ dislocation loops in bcc metals has been proposed by Eyre and Bullough [18] based on shearing of initially formed $a/2\langle 1\,1\,0\rangle$ dislocation loops. TEM observations on irradiated molybdenum and tungsten have provided direct evidence that both interstitial and vacancy loops are nucleated on $\{1\,1\,0\}$ planes consistent with the Eyre–Bullough model although in these cases all loops shear to the expected $a/2\langle 1\,1\,1\rangle$ Burgers vector [19,20]. However, the formation of the $a\langle 1\,0\,0\rangle$ dislocation loops requires a higher energy shear in the Eyre–Bullough mechanism. Recently, Marian and Wirth [21] proposed an alternative mechanism for the nucleation and growth of TEM visible $a\langle 1\,0\,0\rangle$ loops based on molecular dynamics simulations. The $a\langle 1\,0\,0\rangle$ loops are postulated to form as a result of direct interactions of mobile $a/2\langle 1\,1\,1\rangle$ clusters of comparable size. The $a\langle 1\,0\,0\rangle$ loops are stable and practically immobile, allowing for the absorption of other small $a/2\langle 1\,1\,1\rangle$ clusters thereby allowing $a\langle 1\,0\,0\rangle$ loop growth up to TEM observation sizes. This consideration is consistent with our observation that a majority of the analyzed $a\langle 1\,0\,0\rangle$ dislocation loops were 2 nm diameter or larger. However, the mechanism of the formation of $a\langle 1\,0\,0\rangle$ dislocation loops in bcc metals is not fully understood.

The vacancy or interstitial nature of dislocation loops is important for considering the effects on radiation embrittlement. In the present experiment, all observed dislocation loops were too small to observe inside–outside fringes and it was not possible to obtain dynamic two-beam (black–white) images required for stereoscopic analysis of the layer structure of such image [22]. Thus the vacancy or interstitial nature of the dislocation loops has not been determined directly. Nevertheless an indirect method based on the relative stability of vacancy and interstitial loops on annealing has been used to infer the loop nature. Fig. 7 shows a weak-beam image taken in $\boldsymbol{g} = 0\,1\,\bar{1}$ close to the [0 1 1] pole in the foil at a depth of 300 nm after post-irradiation annealing at 400 °C for 30 min. The dislocation loops were observed as white dots. Fig. 8 shows images of the same area imaged (a) with $\boldsymbol{g} = 0\,2\,0$, and (b) $\boldsymbol{g} = 2\,0\,0$ close to the [0 0 1] pole. One of the three loop variants with $\boldsymbol{b} = a\langle 1\,0\,0\rangle$ has $|\boldsymbol{g}\cdot\boldsymbol{b}| = 2$ and should be visible in Fig. 8(a), but this loop variant has $|\boldsymbol{g}\cdot\boldsymbol{b}| = 0$ and should be out-of-contrast in (b). All four loop variants with $b = a/2\langle 1\,1\,1\rangle$ have $|\boldsymbol{g}\cdot\boldsymbol{b}| = 1$ and should be visible in Fig. 8(a) and (b). In Fig. 8(a), the encircled white dots show the dislocation loops with typical $|\boldsymbol{g}\cdot\boldsymbol{b}| > 0$ type contrast. But these dislocation loops are out-of-contrast in Fig. 8(b). This result means that these dislocation loops have

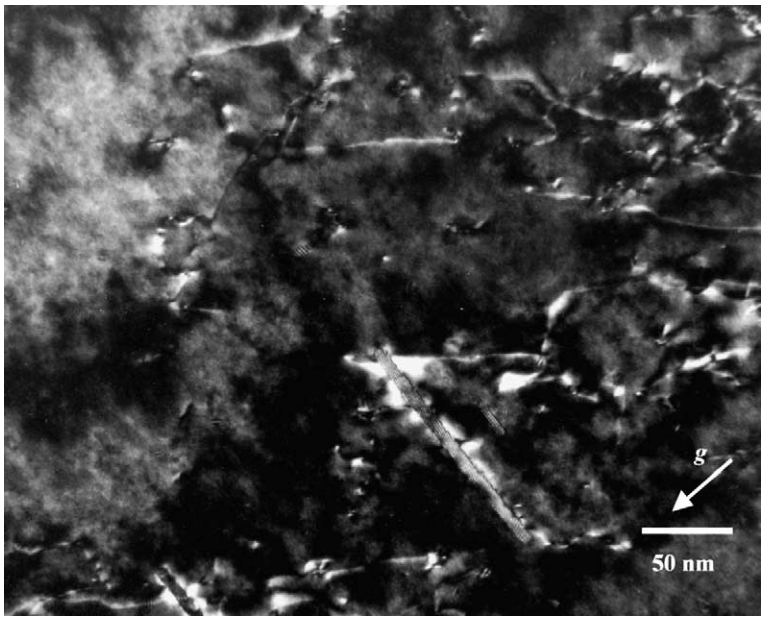

Fig. 7. A weak-beam micrograph taken in $\boldsymbol{g} = 0\,1\,\bar{1}$ close to the [0 1 1] pole in the foil at 300 nm depth after post-irradiation annealing at 400 °C for 30 min.

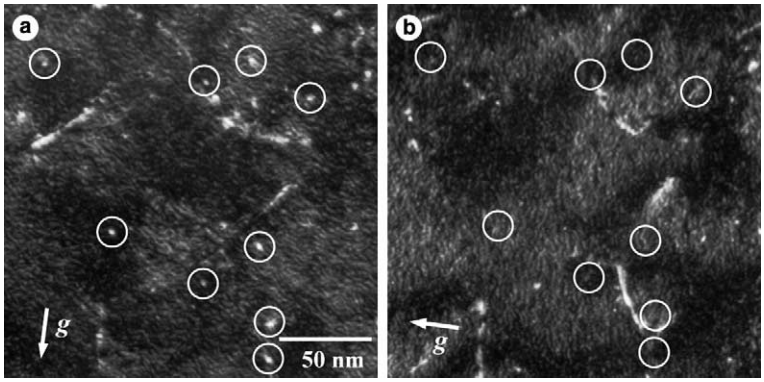

Fig. 8. Contrast analysis on dislocation loops: weak-beam images of the same area imaged (a) with $\boldsymbol{g} = 020$, and (b) $\boldsymbol{g} = 200$ close to the [001] pole, in the foil at 300 nm depth.

$\boldsymbol{b} = a\langle 100\rangle$. Based on the results of the detailed contrast analyses, most of the recognized dislocation loops had $\boldsymbol{b} = a\langle 100\rangle$. Burgers vectors of the dislocation loops did not change under the annealing at 400 °C. The size distribution of the dislocation loops is shown in Fig. 9. The mean image size was $d = 2.2$ nm. The size distribution did not significantly change, but the larger loops such as $d \geqslant 3.5$ nm were not detected after the annealing. Estimates of the dislocation loop number density gave a value of about $7 \times 10^{21}\,\mathrm{m}^{-3}$. This value was slightly lower than that in the as-irradiated samples. If the as-irradiated loop population is of vacancy (or predominantly vacancy) in nature, rapid shrinkage driven by the loop line tension would be expected by vacancy emission [23] and annealing results in loop ripening with the smallest loops shrinking to feed vacancies to the larger loops. This possibility is unlikely because loop growth was not observed. Another possibility is that the as-irradiated loop population is of a mixed vacancy plus interstitial in nature. In this case, the vacancy loops shrink on annealing with the vacancies migrating to the interstitial loops and other sinks, leaving a net interstitial loop population. This possibility is more difficult to rule out. After the annealing, the integrated number and concentration of point defects retained in the visible loops were calculated as $4 \times 10^{23}\,\mathrm{m}^{-3}$ and $\sim 1 \times 10^{-5}$, respectively. The retained point defect concentration in the visible loops slightly decreased on the annealing. This is attributed to absorption of thermal vacancies on the annealing. However, many dislocation loops were stable to a temperature of 400 °C. This indirect evidence suggests that most of the dislocation loops are of interstitial in nature and such an interpretation is also consistent with larger loops being observed adjacent to grain boundaries which act as sinks for vacancies. Hoelzer et al. [9] and Nicol et al. [10] also found $a\langle 100\rangle$ interstitial loops as matrix damage in nearly pure irons irradiated by neutrons to 0.06 dpa at 280 °C, while $a\langle 100\rangle$ interstitial loops were also observed in a mild steel following electron irradiation at 550 °C [16]. Thus there is a body of evidence showing the occurrence of $a\langle 100\rangle$ interstitial loops in irradiated iron and reactor vessel steels.

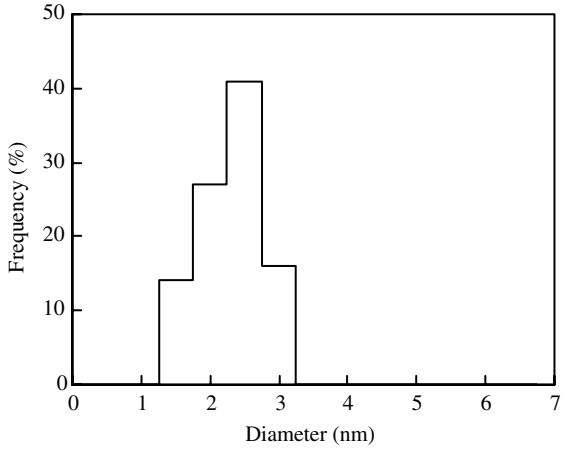

Fig. 9. Size distribution of dislocation loops after post-irradiation annealing at 400 °C for 30 min.

4. Conclusions

1. Matrix damage in A533B steels produced by Ni ion irradiation to a dose of 1 dpa at a temperature of 290 °C consists of small (2–6 nm) dislocation loops.
2. Most of the visible dislocation loops that could be analyzed have $\boldsymbol{b} = a\langle 100\rangle$.
3. The dislocation loops have a mean image size $d = 2.5$ nm and the number density is $1 \times 10^{22}\,\mathrm{m}^{-3}$.
4. Dislocation loops with $\boldsymbol{b} = a\langle 100\rangle$ were also observed after thermal annealing at 400 °C for 30 min. The dislocation loops have $d = 2.2$ nm and the number density is about $7 \times 10^{21}\,\mathrm{m}^{-3}$.

5. The interstitial or vacancy nature of the dislocation loops was not determined directly. However, most of the dislocation loops were stable under thermal annealing at 400 °C. This indirect evidence suggests that their nature is interstitial.

Acknowledgments

We thank Professor Brian Eyre at the University of Oxford for helpful discussions. We also thank Professor John Titchmarsh and Dr Mike Jenkins at the University of Oxford for helpful discussions of TEM observation and analysis.

References

[1] S.B. Fisher, J.E. Harbottle, N. Aldridge, Philos. Trans. Roy. Soc. A 315 (1985) 301.
[2] G.R. Odette, G.E. Lucas, Rad. Eff. Def. Solids 144 (1998) 189.
[3] T.J. Williams, D. Ellis, D.I. Swan, J. McGuire, S.P. Walley, C.A. English, J.H. Venables, P.H.N. de la cour Ray, Proceedings of the 2nd International Symposium on Environmental Degradation of Materials in Nuclear Power Systems – Water Reactors, ANS, 1986, p. 323.
[4] T.J. Williams, P.R. Burch, C.A. English, P.H.N. de la cour Ray, Proceedings of the 3rd International Symposium on Environmental Degradation of Materials in Nuclear Power Systems – Water Reactors, ASME, 1988, p. 121.
[5] B.C. Masters, Philos. Mag. 11 (1965) 881.
[6] B.L. Eyre, A.F. Bartlett, Philos. Mag. 12 (1965) 261.
[7] M.L. Jenkins, C.A. English, B.L. Eyre, Philos. Mag. A 38 (1978) 97.
[8] I.M. Robertson, M.L. Jenkins, C.A. English, J. Nucl. Mater. 108/109 (1982) 209.
[9] D.T. Hoelzer, F. Ebrahimi, Mat. Res. Soc. Symp. Proc. (Materials Research Society) 373 (1995) 57.
[10] A.C. Nicol, M.L. Jenkins, M.A. Kirk, Mat. Res. Soc. Symp. Proc. 650 (2001) R1.3.1.
[11] M.L. Jenkins, M.A. Kirk, H. Fukushima, J. Electron Microsc. 48 (1999) 323.
[12] M.A. Kirk, M.L. Jenkins, H. Fukushima, J. Nucl. Mater. 276 (2000) 50.
[13] J.F. Ziegler, J.P. Biersak, U. Littmark, The Stopping and Range of Ions in Solids, Pergamon, New York, 1985.
[14] P.M. Kelly, A. Jostens, R.G. Blake, J.G. Napier, Phys. Status Solidi a 31 (1975) 771.
[15] B.L. Eyre, D.M. Maher, R.C. Perrin, J. Phys. F: Metal Phys. 7 (1977) 1371.
[16] E.A. Little, B.L. Eyre, Metal Sci. J. 7 (1973) 100.
[17] J.M. Harder, D.J. Bacon, Philos. Mag. A 58 (1988) 165.
[18] B.L. Eyre, R. Bullough, Philos. Mag. A 12 (1965) 31.
[19] F. Housermann, Philos. Mag. 25 (1972) 561.
[20] C.A. English, B.L. Eyre, S.M. Holmes, J. Phys. F: Met. Phys. 10 (1980) 1065.
[21] J. Marian, B.D. Wirth, Phys. Rev. Let. 88 (2002) 255507.
[22] M. Ruhle, M. Wilkens, U. Essman, Phys. Stat. Solidi 11 (1965) 819.
[23] B.L. Eyre, D.M. Maher, Philos. Mag. 24 (1971) 767.